

Three-Component Kinematics of Multiple Stellar Populations in Globular Clusters with Gaia and VLT.

G. CORDONI,¹ A. P. MILONE,¹ A. MASTROBUONO-BATTISTI,² A. F. MARINO,^{1,3} E. P. LAGIOIA,¹ M. TAILO,¹ H. BAUMGARDT,⁴ AND M. HILKER⁵

¹*Dipartimento di Fisica e Astronomia “Galileo Galilei” - Univ. di Padova, Vicolo dell’Osservatorio 3, Padova, IT-35122*

²*Max-Planck Institut für Astronomie, Königstuhl 17, D-69117 Heidelberg, Germany*

³*Centro di Ateneo di Studi e Attività Spaziali “Giuseppe Colombo” - CISAS, Via Venezia 15, Padova, IT-35131*

⁴*School of Mathematics and Physics, The University of Queensland, St. Lucia, QLD 4072, Australia*

⁵*European Southern Observatory, Karl-Schwarzschild-Str 2, D-85748 Garching, Germany*

(Accepted 21/11/2019)

Submitted to ApJ

ABSTRACT

The internal dynamics of multiple stellar populations in Globular Clusters (GCs) provides unique constraints on the physical processes responsible for their formation. Specifically, the present-day kinematics of cluster stars, such as rotation and velocity-dispersion, could be related to the initial configuration of the system. In recent work, we provided the first study of the kinematics of different stellar populations in NGC 0104 over a large field of view in the plane of the sky, exploiting Gaia Data Release 2 (DR2) proper motions combined with multi-band ground-based photometry.

In this paper, we combine Gaia DR2 proper motions with Very Large Telescope radial velocities to investigate the kinematics along the line of sight and in the plane of the sky of multiple populations in seven GCs, namely NGC 0104, NGC 0288, NGC 5904, NGC 6121, NGC 6254, NGC 6752 and NGC 6838. Among the analyzed clusters only NGC 0104 and NGC 5904 show significant rotation.

Separating our sample into two groups of first- and second-population stars (1P and 2P) we find that overall these two populations exhibit a similar rotation pattern in NGC 0104. However, some hints of different rotation are observed in the external regions of this cluster. Interestingly, 1P and 2P stars in NGC 5904 show different rotation curves, with distinct phases and such difference is significant at the $\sim 2.5\text{-}\sigma$ level. The analysis of the velocity-dispersion profiles of multiple populations confirms that 2P stars of NGC 0104 show stronger anisotropy than the 1P.

Keywords: globular clusters: general, stars: population II, stars: abundances, dynamics, techniques: photometry.

1. INTRODUCTION

Studies based on *Hubble Space Telescope* (*HST*) images revealed that the photometric diagrams of nearly all GCs are composed of two main groups of first- and second-population stars (1P, 2P, e.g. Milone et al. 2017) with different chemical compositions (e.g. Marino et al. 2019). Many efforts have been made to understand their origin, but, so far, none of the proposed scenarios have been able to reach a satisfactory agreement with observations (e.g. Renzini et al. 2015). According to many of these scenarios, 2P stars formed out of

the ejecta of 1P more-massive stars (e.g. Ventura et al. 2001; Decressin et al. 2007; D’Ercole et al. 2010; Denissenkov & Hartwick 2014) after the segregation of the gas in the cluster center. As a consequence, 2P stars may have formed in a more centrally-concentrated environment.

As an alternative hypothesis, GCs host a single stellar generation and stars with different chemical composition are the product of exotic physical phenomena specific of proto-GCs (e.g. de Mink et al. 2009; Bastian et al. 2013; Gieles et al. 2018).

An important signature of the physical processes responsible for the formation of multiple populations is the kinematics of cluster stars. Specifically, N -body simulations suggest that the dynamical evolution of more centrally-concentrated 2P stars should be significantly different from that of 1P stars,

and such difference could still be observable in present-day GC kinematics (e.g. [Vesperini et al. 2013](#); [Mastrobuono-Battisti & Perets 2013, 2016](#); [Hénault-Brunet et al. 2015](#); [Tiongco et al. 2019](#)).

In the past decade, nearly all works on the internal kinematics of GCs were based on radial velocities of a relatively-small sample of stars (e.g. [Norris et al. 1997](#); [Bellazzini et al. 2012](#); [Marino et al. 2014](#); [Cordero et al. 2014](#)) with the study of 650 stars of NGC 5139 (ω Centauri) by [Pancino et al. \(2007\)](#), being a remarkable exception.

More recently, *HST* provided high-precision relative proper motions of a small but increasing number of clusters, namely NGC 0104 (47 Tucanae), NGC 0362, NGC 2808, NGC 5139 and NGC 6352 that allowed the investigation of the kinematics of multiple populations in the plane of the sky ([Richer et al. 2013](#); [Bellini et al. 2015, 2018](#); [Libralato et al. 2018, 2019](#)). In all the studies the authors concluded that 2P stars show a more-radially anisotropic velocity distribution. While these works are based on high-precision relative proper motions of thousands of stars, the small field of view of *HST* does not allow the study of the entire cluster.

To overcome this shortcoming and study the kinematics of multiple stellar populations over a large field of view, we started a project based on Gaia Data Release 2 (DR2¹, [Gaia Collaboration et al. 2018a](#)) accurate proper motions and multi-band wide-field ground-based photometry. In the pilot paper of this project, we investigated for the first time the kinematics of 1P and 2P stars of NGC 0104 over a wide field of view, up to ~ 18 arcmin from the cluster center (corresponding to ~ 22 pc, [Milone et al. 2018](#)). In the present work, we analyse the spatial distributions and the 3D kinematics of NGC 0104 and other six GCs, namely NGC 0288, NGC 5904 (M 5), NGC 6121 (M 4), NGC 6254 (M 10), NGC 6752 and NGC 6838 (M 71), whose physical parameters are listed in Table 1.

The paper is organized as follows: in Section 2 we introduce the dataset and present the photometric diagrams of the analyzed clusters. In Section 3 we analyze the spatial distribution of multiple stellar populations. The 3D rotation of 1P and 2P stars and their velocity dispersion are investigated in Sections 4 and 5, respectively. Finally, Section 6 provides the summary and the discussion of the results.

2. DATA AND DATA ANALYSIS

To investigate the internal kinematics of multiple stellar populations in each GC, we combined ground-based wide-field photometry, proper motions from Gaia DR2 and high-precision radial velocities provided by [Baumgardt & Hilker \(2018\)](#) and derived from archival ESO/VLT and Keck spectra together with published radial velocities from the literature.

Photometry in U , B , V , I bands has been derived by Peter Stetson from images collected with various facilities and by using the methods and the computer programs by [Stetson \(2005\)](#) and [Stetson et al. \(2019\)](#). Photometry has been calibrated on the reference system by [Landolt \(1992\)](#). Details on the dataset and on the data reduction are provided by [Monelli et al. \(2013\)](#) and [Stetson et al. \(2019\)](#). The photometric catalogs by Stetson and collaborators have been widely used to investigate multiple populations in GCs (e.g. [Monelli et al. 2013](#); [Marino et al. 2016, 2017](#); [Milone et al. 2012, 2018](#); [Stetson et al. 2019](#)). Most of these works are based on the pseudo color $C_{U,B,I} = (U - B) - (B - I)$, which is an efficient tool to identify stellar populations with different light-element abundance along the RGB and will be used in the following to identify 1P and 2P stars. We corrected proper motions for the perspective expansion/contraction due to the bulk motion of the GC by means of Equation 6 in [van den Ven et al. \(2006\)](#).

As well established in the literature, Gaia DR2 proper motions suffer from systematic errors that mostly depend on stellar colors and positions (e.g. [Gaia Collaboration et al. 2018a](#); [Bianchini et al. 2018](#); [Lindegren et al. 2018](#); [Sollima et al. 2019](#); [Vasiliev 2019a,b](#)). In this work we are interested in the relative motions of groups of 1P and 2P stars that are almost indistinguishable to the eye of Gaia, as they have similar colors and magnitudes and, to a first approximation, share the same spatial distributions. As a consequence, the systematic errors associated with the motions of both populations are similar and their effects on the relative motions of 1P and 2P stars may be cancelled out when infinite amounts of 1P and 2P stars are available. However, in the case of finite numbers of stars the effect of systematics on the relative proper motions of the two populations may not entirely cancel out. In this work, we used a conservative approach and followed the recipe described in [Vasiliev \(2019b\)](#)² to entirely account for systematic errors in our analysis of 1P and 2P stars. Since we are considering relative motions, our error estimates would overestimate the true uncertainties.

2.1. Selection of cluster members

To study the kinematics of stellar populations in GCs we need accurate stellar proper motions. To identify a sample of RGB stars with high-quality astrometric measurements we exploited the method used by [Milone et al. \(2018\)](#) and [Cordoni et al. \(2018\)](#), which is illustrated in Figure 1 for NGC 6838, and exploits the parameters provided by the Gaia DR2.

In a nutshell, we first selected a sample of stars with high-accuracy proper motions, by using the `astrometric_gof_al`

¹ <https://gea.esac.esa.int/archive/>

² code publicly available at <https://github.com/GalacticDynamics-Oxford/GaiaTools>

(*As_gof_al*) parameter, indicative of the goodness of fit statistics of the astrometric solution for the source in the along-scan direction (see [Gaia Collaboration et al. 2018a](#), for details), and the renormalized unit weight error ([Lindegren et al. 2018](#)). To do this, we divided the G_{RP} -magnitude range between 11.0 and 18.5 into bins of 0.5 mag. We calculated the median magnitude ($G_{\text{RP},i}$), the median *As_gof_al* value (As_gof_al_i) and the corresponding random mean scatter (σ_i) for stars in each magnitude bin (i). We associated the values of $G_{\text{RP},i}$ and $\text{As_gof_al}_i + 4 \sigma_i$ and linearly interpolated these points to derive the green line of Figure 1a. We considered those stars that lie on the left side of the green line as well measured. Moreover, only stars with proper motion uncertainties smaller than 0.35 mas/yr have been included in our analysis.

We determined cluster membership of each star using the same procedure described in [Cordoni et al. \(2018, see their Section 2\)](#). Briefly, we analyzed the proper motion vector-point diagram (VPD) shown in panel d of Figure 1, and derived by eye a circle enclosing most cluster stars. Then, we calculated the proper motion of each star relative to the cluster mean motion (μ_{R}). We plotted μ_{R} against the G_{RP} -magnitude and selected only stars with dispersion lower than 4σ from the mean relation. We then repeated the same procedure for the parallax, π . This procedure has been iterated three times. We verified that the sample of cluster stars identified from the criteria described above is nearly coincident with that obtained by following the method by [Vasiliev \(2019a\)](#), which is based on Gaussian mixture models. When we adopt the latter stellar sample the conclusions of the paper remain unchanged.

As a final step, the U , B , V , I photometry of cluster members has been corrected for differential reddening using the method described in ([Milone et al. 2012, see their Section 3.1](#)). In a nutshell, we first derived the fiducial line of MS and SGB stars in the I vs. $(B-I)$ plane, where 1P/2P stars are almost indistinguishable, and we calculated the residuals from this line. Then we selected 35 neighbors MS and SGB bright cluster members and computed the median of the color-residuals, calculated along the reddening direction, as our differential-reddening estimate. In panels e and f of Figure 1 we compare the original I vs. $(B-I)$ CMD of NGC 6838 members and the corresponding CMD corrected for differential reddening. Clearly, the comparison between the original and the differential-reddening free CMD suggests that our correction provides much narrower photometric sequences, demonstrating the goodness of our procedure.

2.2. Multiple populations along the color-magnitude diagrams

To distinguish 2P from 1P stars we exploit photometric diagrams based on the $C_{\text{U,B,I}}$ index. Indeed, a visual inspec-

tion of our V vs. $C_{\text{U,B,I}}$ diagrams of cluster members, reveals that 1P and 2P stars of the analyzed GCs define two distinct RGBs (see also [Monelli et al. 2013; Marino et al. 2016, 2017; Milone et al. 2012, 2018](#)).

The procedure that we used to identify the sample of 1P and 2P stars is illustrated in Figure 2 for NGC 6838 and is based on the V vs. $C_{\text{U,B,I}}$ diagram plotted in panel a. The red and blue lines superimposed on the diagram correspond to the RGB boundaries and are derived as in [Milone et al. \(2017, see their Section 3\)](#). In the case of NGC 6838 we only used stars in the magnitude interval between $V=12.0$ and $V=17.5$, where the RGB split is clearly visible. In a nutshell, we first divided the magnitude interval between $V=14.0$ and $V=17.5$ into a series of bins of size $dV = 0.9$ mag. The bins are defined over a grid of points separated by 0.3 mag. For each bin we calculated the average V magnitude and associate its value to the 4th and the 96th percentile of the $C_{\text{U,B,I}}$ distribution of RGB stars. We smoothed these points by using boxcar averaging, where we substituted each point with the average of its three adjacent points. Due to the small number of stars brighter than $V = 14.0$, the fiducial points of the portion of the RGB with $12.0 \lesssim V \lesssim 14.0$ are drawn by eye.

The fiducial lines are verticalized as in [Milone et al. \(2015, see their Section 3.1\)](#) to derive the V vs. $\Delta C_{\text{U,B,I}}$ diagram plotted in panel b. Panel c of Figure 2 shows the histogram and the kernel-density distribution of the $\Delta C_{\text{U,B,I}}$ for RGB stars with $12.0 < V < 17.5$. Clearly, the $\Delta C_{\text{U,B,I}}$ distribution represented in panels b and c allows us to distinguish 1P stars (represented with red circles) from 2P stars (blue triangles), based on the vertical dashed line.

The same procedure illustrated for NGC 6838 has been applied to the other six clusters that we have analyzed. Figure 3 shows the V vs. $C_{\text{U,B,I}}$ diagrams and the corresponding $\Delta C_{\text{U,B,I}}$ histograms and kernel-density distributions of RGB stars for NGC 0104, NGC 0288, NGC 5904, NGC 6121, NGC 6254 and NGC 6752. The RGB of each cluster defines two distinct sequences and allows us to select the groups of 1P (red dots) and 2P stars (blue triangles). Only the selected 1P and 2P RGB stars will be used to explore the kinematics of multiple populations in each GC. In NGC 0104 and NGC 6838, we included in the analysis 1P and 2P HB stars that we selected from the $U - B$ vs. $B - I$ two-color diagram as in [Milone et al. \(2012\)](#).

3. SPATIAL DISTRIBUTION

In the following, we analyze the spatial distribution of the two groups of 1P and 2P stars that we identified in the previous section for the seven analyzed clusters. To do this, we used a procedure, which is based on the 2D Binned Kernel Density Estimate ([Wand 2015](#)), illustrated in the left and right panels of Figure 4 for the first and second population of NGC 5904, respectively. The levels of red and blue in the up-

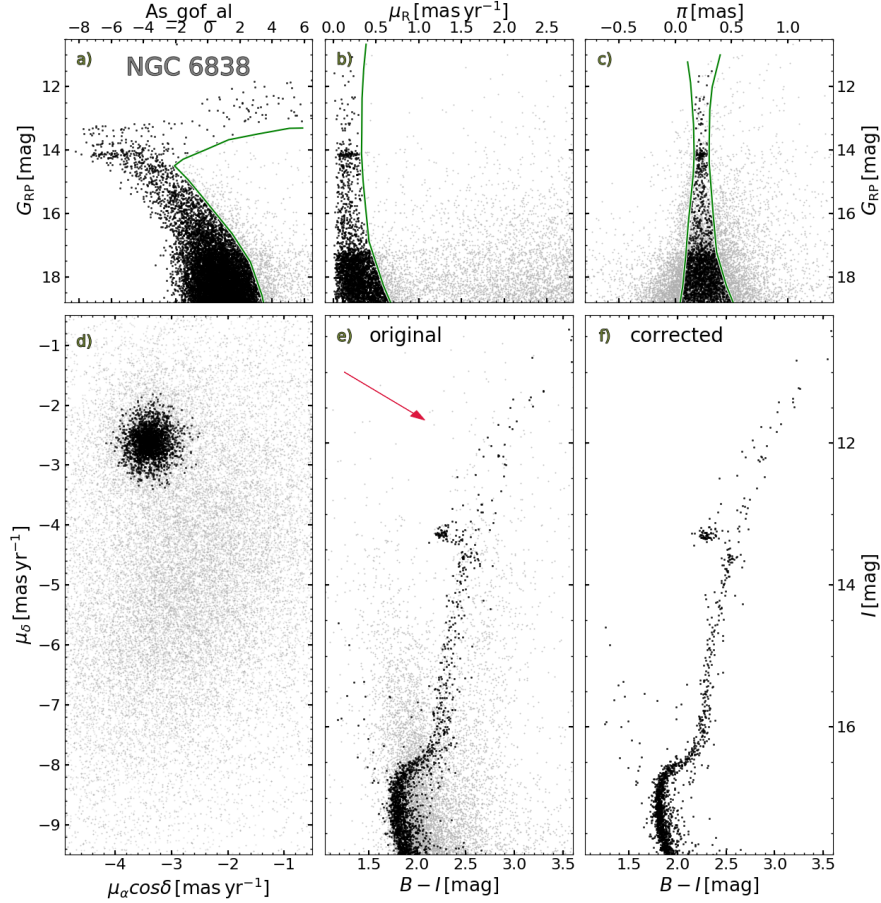


Figure 1. Illustration of the procedure to select stars with high-quality proper motions and to determine the *bona-fide* cluster members of NGC 6838. Panels a, b, and c show the G_{RP} magnitude from Gaia DR2 against the As_gof_al parameter, stellar proper motions relative to the cluster mean motion, μ_{R} , and parallax, π , respectively. The green lines separate cluster members (black points) from field stars (gray points). The proper motion vector-point diagram is plotted in panel d. Panels e and f compare the original I vs. $B - I$ CMD of cluster members with the CMD corrected for differential reddening. The red arrow in panel e represents the reddening vector and corresponds to a reddening variation of $E(B - V) = 0.3$. See text for details.

per panels are indicative of the density of 1P and 2P stars in a reference frame where the origin corresponds to the cluster center and the X and Y axes point towards the directions of increasing RA and DEC.

We calculated six and nine iso-density contour lines for 1P and 2P respectively, spaced by 0.001 in normalized density unit (black lines in the upper panel). We used the algorithm by Radim & Flusser (1998) to fit each contour line with an ellipse by means of least-squares and plot the best-fit ellipses in the bottom-left panel of Figure 4, where we also show the corresponding directions of the major axes. A visual inspection of Figure 4 suggests that 2P stars exhibit more-elongated distributions than the 1P. To quantify this fact, we define the ellipticity as $e = 1 - b/a$ where a, b are respectively the semi-major and semi-minor axis of the interpolated ellipses.

The ellipticity radial profile is presented in Figure 5. The

uncertainty associated with each ellipticity measurement is determined by means of bootstrapping 1,000 times with replacement. Clearly, 2P stars exhibit larger values of e than the 1P, as previously found in Lee (2017). The ellipticity difference between 2P and 1P decreases from $\Delta(e) \sim 0.1$, at a radial distance of about 1 arcmin ($\sim 0.61 R_{\text{h}}$, ~ 2 pc) from the cluster center, to ~ 0.02 for $a \sim 8$ arcmin ($\sim 4.7 R_{\text{h}}$, ~ 17 pc).

To estimate the statistical significance of $\Delta(e)$ we sampled the observed radial profile of the cluster to create a catalog of 100,000 stars with a radial distribution similar to the observed ones and with ellipticity $e = 0$. We selected two stellar groups with the same number of stars as observed for the 1P and the 2P, derived their ellipticity at different radial distances from the center and calculated Δe_{sim} in close analogy with what we did for the observed stars. Finally, we computed the ratio between the number of simulations where

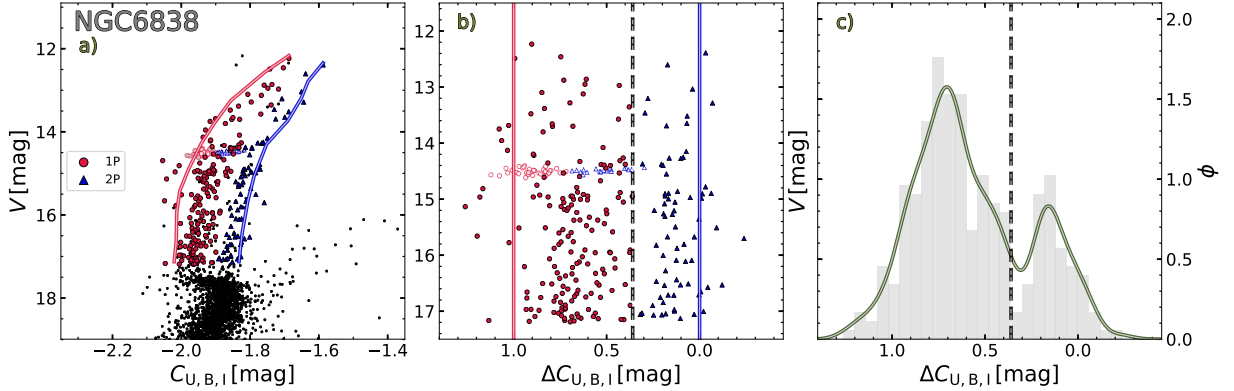


Figure 2. This figure illustrates the procedure to select 1P and 2P stars along the RGB of NGC 6838. Panel a shows the V vs. $C_{U,B,I}$ diagram for cluster members, while the verticalized V vs. $\Delta C_{U,B,I}$ diagram for RGB stars and the corresponding $\Delta C_{U,B,I}$ histogram distribution are plotted in panel b and c, respectively. The red and blue continuous lines mark the boundaries of the RGB, while the dashed gray vertical line is used to separate 1P (red circles) stars from 2P stars (blue triangles). HB stars are marked with empty symbols. The continuous line superimposed on the histogram represents the $\Delta C_{U,B,I}$ kernel-density distribution of RGB stars. See text for details.

ID	RA (J2000) ^a	DEC (J2000) ^a	mass ^b [M_{\odot}]	d_{sun}^b [kpc]	R_{Gal}^a [kpc]	R_c^b [arcmin]	R_h^b [arcmin]	\bar{V}_{LoS}^b [km/s]	$\log \tau_{\text{RH}}^b$ yr
NGC 0104	00 24 05.67	-72 04 52.6	7.79×10^5	4.41	7.40	0.38	2.78	-17.20	9.58
NGC 0288	00 52 45.24	-26 34 57.4	1.16×10^5	9.80	12.0	1.67	2.45	-44.83	9.58
NGC 5904	15 18 33.22	+02 04 51.7	3.72×10^5	7.50	6.20	0.55	1.65	53.70	9.45
NGC 6121	16 23 35.22	-26 31 32.7	9.69×10^4	2.14	5.90	1.06	4.53	71.05	8.99
NGC 6254	16 57 09.05	-04 06 01.1	1.84×10^5	4.71	4.60	0.59	2.03	74.02	9.15
NGC 6752	19 10 52.11	-59 59 04.4	2.39×10^5	4.30	5.20	0.15	1.92	-26.28	9.16
NGC 6838	19 53 46.49	+18 46 45.1	4.91×10^4	3.86	6.70	0.46	2.63	-22.27	8.90

^afrom Harris (1996, updated as in 2010)

^bfrom Baumgardt & Hilker (2018)

Table 1. Identification, positional data and adopted structural parameters for the analyzed clusters. For each cluster we list position (RA, DEC), distance from the Sun, galactocentric radius (R_{Gal}), mass, core radius (R_c), half-light radius (R_h), line-of-sight mean velocity (\bar{V}_{LoS}) and half-mass relaxation time ($\log \tau_{\text{RH}}$).

$\Delta e_{\text{sim}} \geq \Delta e$ and the total number of simulations. This quantity corresponds to the probability that the observed ellipticity difference between 2P and 1P stars is not due to observational uncertainties. As shown in the inset of Figure 5, where we plot Δe against the semi-major axis of the corresponding the best-fit ellipse, the significance of the ellipticity difference between the stellar populations of NGC 5904 ranges from more than 90% in the innermost regions, to $\sim 60\%$ for $a \sim 8$ arcmin.

Results for the other clusters are shown in Figure 6. We find significant differences in the spatial distribution of 1P and 2P stars in NGC 0104, NGC 5904 and NGC 6254. The remaining clusters do not show hints of different distribution between both populations. It is worth mentioning that while NGC 5904 and NGC 6254 are consistent with a more ellip-

tical 2P, NGC 0104 shows the opposite trend, with a more elliptical 1P.

4. ROTATION OF MULTIPLE POPULATIONS.

In the following, we investigate the rotation in the plane of the sky and along the line-of-sight (LoS) for the selected 1P and 2P stars by using the procedure illustrated in Figure 7 for NGC 5904. We applied the orthographic projection of the celestial coordinates and converted proper motions by using Equation 2 from Gaia Collaboration et al. (2018b).

In the left panel of Figure 7 we plotted the positions of the selected 1P and 2P stars relative to the cluster center and defined the angle θ . In the right panels of the same figure we show the density diagrams of the proper-motion and LoS velocity components ($\mu_{\alpha} \cos \delta, \mu_{\delta}, V_{\text{LoS}}$) of each population against θ . We divided the field of view in sixteen circular sectors with arc length of 45° by using a method based on

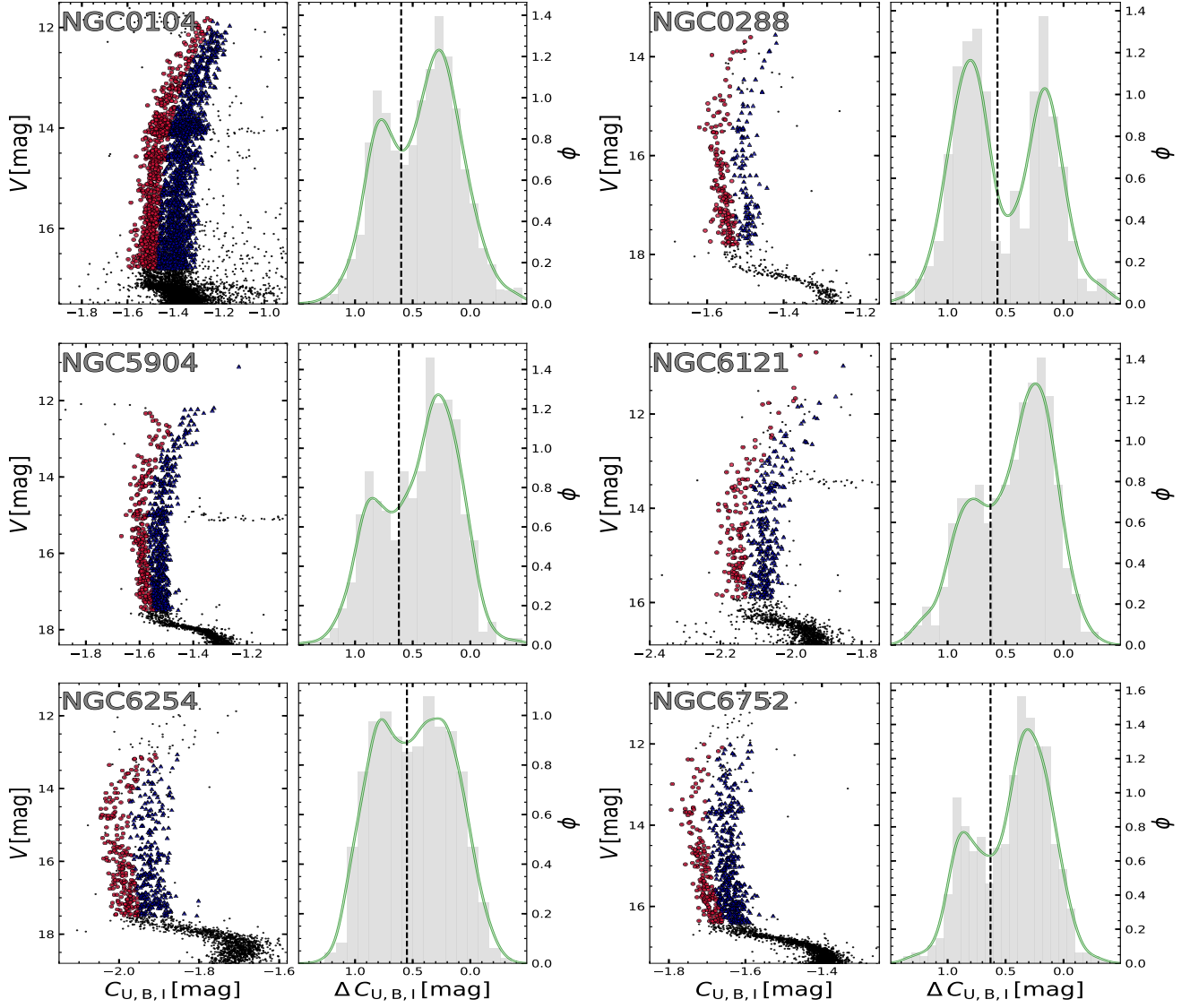


Figure 3. V vs. $C_{U,B,I}$ diagrams for the selected cluster members of NGC 0104, NGC 0288, NGC 5904, NGC 6121, NGC 6254 and NGC 6752 (left panels). The panels on the right show the histogram and the kernel-density $\Delta C_{U,B,I}$ distributions for the RGB stars that we used to investigate the internal kinematics of stellar populations. The vertical dashed lines separate the selected 1P and 2P stars that are colored red and blue, respectively, in the left-panel diagrams.

the naive estimator (Silverman 1986). Specifically, we defined a series of points separated by arc length of $l = 45^\circ$. The circular sectors are defined over a grid of points that are separated by steps of $l/2$ in arc length. We calculated the median proper motions and angular positions of stars in each circular sector. The median values are superimposed on the density plots in the right panels of Figure 7.

A visual inspection of this figure reveals that the proper motions of both 1P and 2P stars of NGC 5904 exhibit sinusoidal patterns, thus suggesting that both populations are rotating.

To investigate the rotation of 1P and 2P stars of all the GCs, we calculated the quantities $\Delta\mu_\alpha \cos\delta$, $\Delta\mu_\delta$ and ΔV_{LoS} respec-

tively corresponding to the difference between the $\mu_\alpha \cos\delta$, μ_δ and V_{LoS} of each star, and the cluster median motion. Results are shown in Figure 8 where we plot for each cluster the median values of $\Delta\mu_\alpha \cos\delta$, $\Delta\mu_\delta$ and ΔV_{LoS} calculated in sixteen circular sectors as a function of θ . This analysis suggests that NGC 0104 and NGC 5904 are the only two clusters with clear evidence of rotation among both 1P and 2P stars. Remarkably, 1P and 2P stars follow the same random pattern in all the clusters with the possible exception of NGC 5904³.

³ Work based on N-body simulations (e.g. Vesperini et al. 2013; Mastrobuono-Battisti & Perets 2016; Tiongco et al. 2019) suggest that the force of rotation should vary within the cluster field, as a function of radial

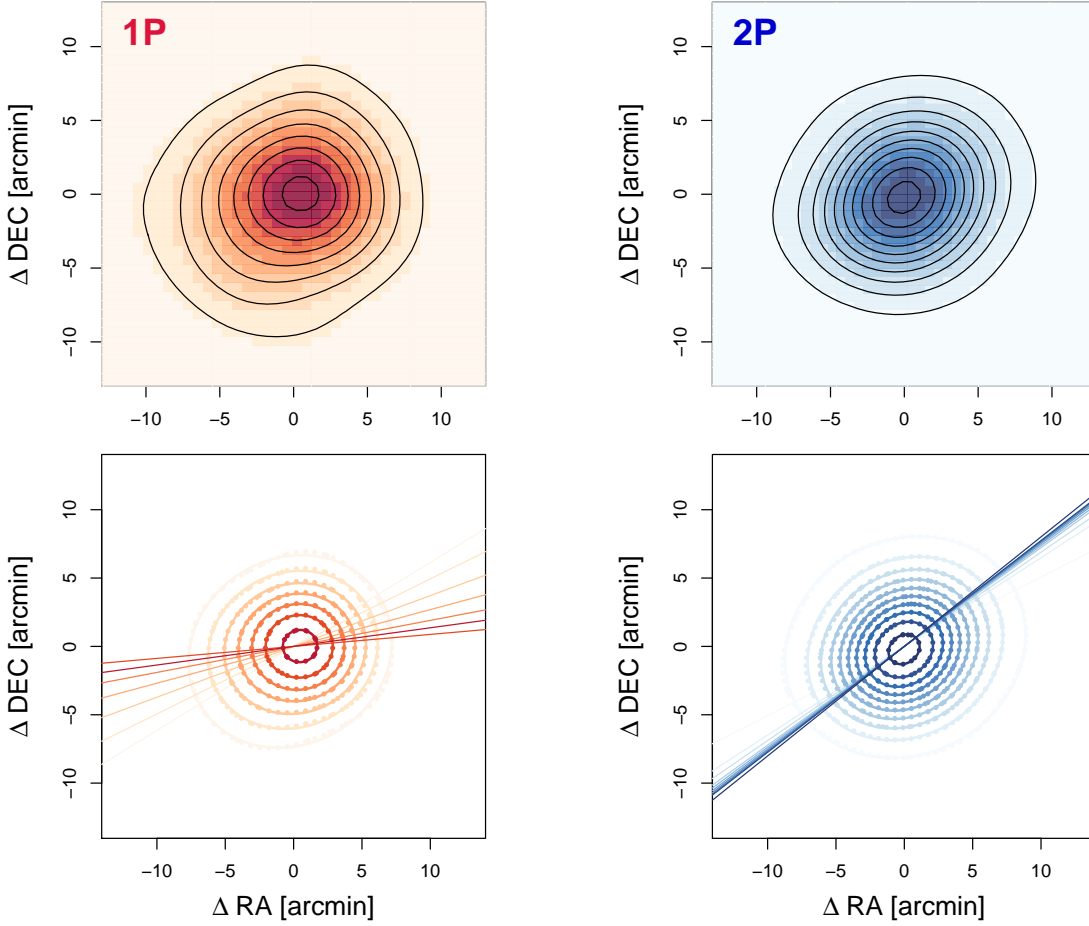


Figure 4. Spatial distribution of multiple stellar populations in NGC 5904. *Top panels.* 2D Binned Kernel Density Estimate (Wand 2015) with iso-density contour lines. *Bottom panels.* Least squares fit ellipses to the iso-density contours. The ellipses have been interpolated using the algorithm described in Halir & Flusser (1998).

To quantify the rotation of each population of NGC 0104 and NGC 5904 and estimate its amplitude, A , and phase, ϕ , we performed least-squares fitting to all 1P and 2P stars of the function:

$$f(\theta) = M + A \cdot \sin(F \cdot \theta + \phi) \quad (1)$$

where M is the zero point of the sine function and F is the frequency. We exploit the r^2 parameter (Glantz 1990) to estimate the statistical significance of the fit:

$$r^2 = 1 - \frac{\sum_i (y_i - f(\theta, i))^2}{\sum_i (f(\theta, i) - \bar{y})^2} \quad (2)$$

where y_i is the value of $\mu_\alpha \cos \delta(\mu_\delta)$ for each star, i , θ is the corresponding position angle, \bar{y} is the average value of y , and

distance. Due to the small number of available 1P and 2P stars in each GC, we performed a global analysis that is based on the rotation of stars at different radial distances from the cluster center. NGC 0104 is the only cluster that contains a sufficient number of stars to study rotation in different radial bins, as discussed in Section 4.1.

f is the best-fit function. This parameter quantifies the goodness of the fit of a linear function, with the perfect match corresponding to $r^2 = 1$. We then eye-checked every cluster for consistency between the interpolation and the value of r^2 .

The values of r^2 for NGC 0288, NGC 6121, NGC 6254, NGC 6752 and NGC 6838 are smaller than 0.5 thus demonstrating that the observations are poorly reproduced by Equation 1. Hence, there is no evidence for rotation among 1P and 2P stars of these clusters.

In contrast, NGC 0104 and NGC 5904 exhibit a reliable match between the function of Equation 1 for both populations. The obtained r^2 values for 1P and 2P stars are listed in the bottom right insets of Figure 8 and are larger than 0.6. The best-fit functions to all 1P and 2P stars for these two clusters are shown in Figure 8.

Once established that 1P and 2P stars of NGC 0104 and NGC 5904 rotate, we can further explore the rotation pattern of different stellar populations in these two clusters.

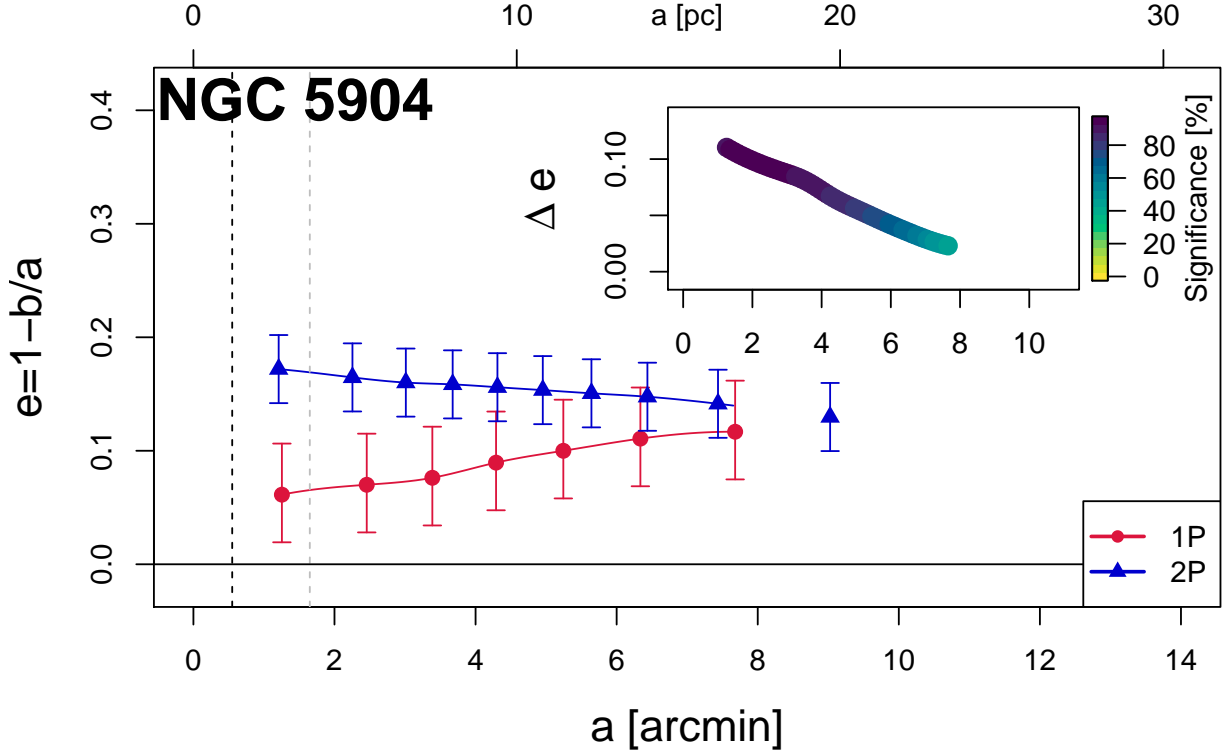


Figure 5. Ellipticity, e , of 1P and 2P (color coded in red and blue respectively) as a function of the semi-major axis, a . Black and gray dashed lines indicate the core radius (R_c) and the half-light radius (R_h), respectively. The inset shows the ellipticity difference between 2P and 1P stars, Δe against a . The colors indicate the significance of such difference, as indicated in the colorbar on the right. See text for details.

The values of A and ϕ that provide the best-fit to the observations of NGC 0104 and NGC 5904 are listed in Table 2. In both GCs the zero point, M , is consistent with zero within 0.01 (mas/yr for the proper motion components and km/s for the LoS velocity) and the frequency F is consistent with 1.00 within 0.01 as expected for stellar rotation in GCs.

To estimate the uncertainties on the amplitude and the phase of the sine function that best reproduces the distribution of 1P (2P) stars of each cluster in both proper motions components, we adopted a procedure based on 1,000 Monte Carlo simulations. In each simulation, we generated a sample of N stars with the same θ distribution of the observed 1P (2P) stars. Here N is the number of analyzed 1P (2P) stars.

We used Equation 1 to calculate the value of $f(\theta_i)$ that corresponds to each simulated star, i , by assuming the values of A and ϕ listed in Table 2. Then, we added to $f(\theta_i)$ the same uncertainties that we inferred from the observations, and interpolated the simulated distribution of stars in $\Delta\mu_\delta$ vs. θ ($\Delta\mu_\alpha \cos \delta$ vs. θ , ΔV_{LoS} vs. θ) with Equation 1 by means of least-squares, thus estimating the values of A and ϕ .

We calculated the differences between the 1,000 determinations of A and the true value and assumed the 68.27th percentile of the distribution of the absolute values of these differences as the uncertainty on the determination of A . Similarly, we defined the error associated with the best-fit phase.

To further compare the distributions of 1P and 2P stars in the $\Delta\mu_\alpha \cos \delta$ vs. θ and $\Delta\mu_\delta$ vs. θ planes we used the k-sample Anderson-Darling test (Scholz et al. 1987), which provides the probability of two populations to belong to the same parent distribution. In NGC 0104, NGC 0288, NGC 6121, NGC 6254, NGC 6752 and NGC 6838, 1P and 2P stars have probability $p \geq 0.15$ to come from the same parent distribution. Hence, we conclude that there is no significant difference between the distributions of stellar populations of these clusters. NGC 5904 represents a remarkable exception. Indeed the k-sample Anderson-Darling test provides probabilities of 0.05, 0.03 and 0.16 that the distributions of 1P and 2P stars in the $\Delta\mu_\alpha \cos \delta$ vs. θ , $\Delta\mu_\delta$ vs. θ and ΔV_{LoS} vs. θ planes are drawn from the same distribution. Noticeably, the large difference between the phases of the curves that best-fit 1P and 2P stars in the $\Delta\mu_\delta$ vs. θ plane suggests that the two populations of this cluster exhibit different rotation patterns.

We finally determined the PA of the rotation axis of NGC 0104 and NGC 5904 from the line-of-sight velocity curves as the angle corresponding to a zero LoS velocity. The PAs of the 1P and 2P, marked with red and blue arrows respectively, are shown in the bottom panels of Figure 8 and their values are listed in Table 2. Our results suggest that multiple stellar populations in NGC 5904 do not share the same rotation axis, with the PA of the 1P differing from that

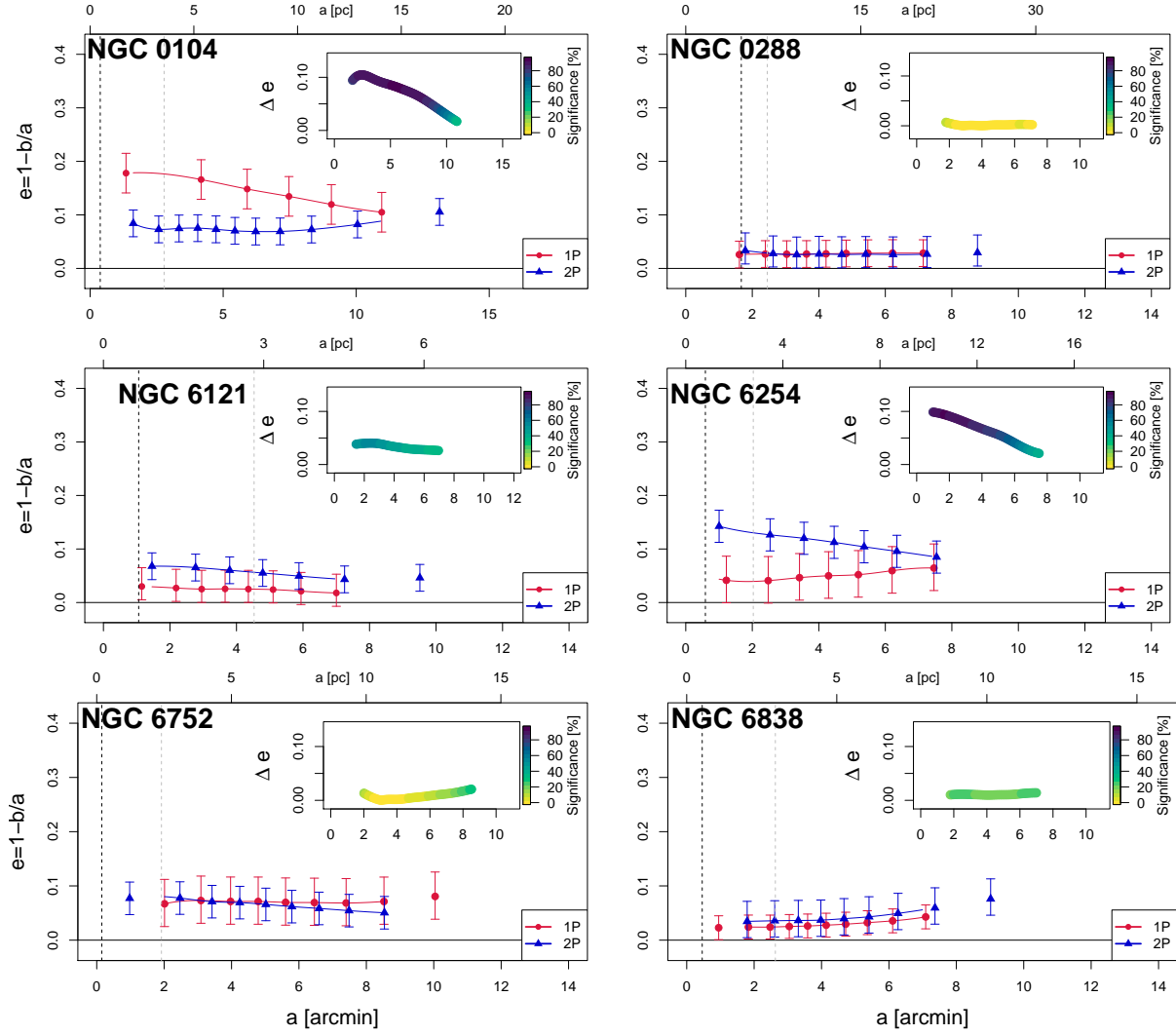


Figure 6. Same as Figure 5 for NGC 0104, NGC 0288, NGC 6121, NGC 6254, NGC 6752 and NGC 6838.

of the 2P by $31^\circ \pm 12^\circ$. On the other hand, NGC 0104 does not show significant differences in the rotation curves of 1P and 2P stars.

4.1. Comparing the rotation of first- and second-population stars in NGC 5904 and NGC 0104

To further investigate whether the difference in the rotation patterns of 1P and 2P stars of NGC 5904 is significant or not, we analyzed 1,000 Monte Carlo realizations, for both 1P and 2P stars. First, we assumed that both populations follow the same proper-motion and LoS-velocity distribution, and estimate the probability that the observed phase and amplitude differences between the corresponding rotation curves is entirely due to observational errors. We simulated two samples of stars with the same angular distribution and the same number of stars as the observed 1P and 2P stars. We associated to each star the value of $\Delta\mu_\alpha \cos \delta$ ($\Delta\mu_\delta$, ΔV_{LoS}) corresponding

to the sine function that provides the best fit with the observations of 2P stars, $f(\theta_i)$ (see Table 2). This procedure ensures that, by construction, the simulated 1P and 2P stars belong to the same parent distribution. Finally, we added the corresponding observational errors to the simulated proper motions of each star, and fitted the resulting distributions of 1P and 2P stars with the function provided by Equation 1. We calculated the difference between the phases ($\Delta\phi$) and the amplitudes (ΔA) derived for 2P and 1P stars and analyzed the distributions of the corresponding absolute values. Results are summarized in Table 3.

We find that the fraction of simulations where the value of $|\Delta\phi|$ obtained from the $\Delta\mu_\delta$ vs. θ plane is equal or larger than the observed phase difference between 2P and 1P stars is 0.008. Hence, the observed phase difference between the curves of the two stellar populations of NGC 5904 is significant at the $\sim 2.6\sigma$ level. In the ΔV_{LoS} vs. θ plane the phase difference has significance of $\sim 2.3\sigma$. On the other hand, we

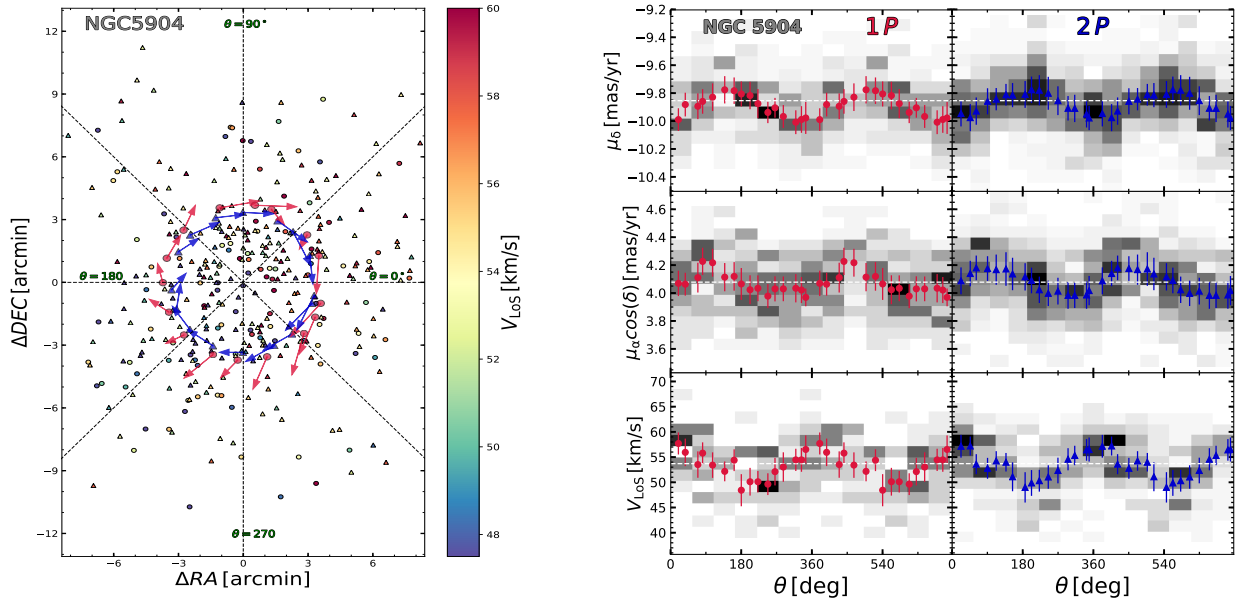


Figure 7. *Left.* Relative position of the analyzed RGB stars of NGC 5904 with respect to the cluster center. 1P and 2P stars are shown with circles and triangles, while the color is representative of the LoS velocity as shown in the colorbar. The red and blue arrows indicate the average rotation field, in the plane of the sky, of 1P stars and 2P stars for the 16 analyzed circular sectors. *Right.* $\mu_\alpha \cos \delta$, μ_δ and V_{LoS} as a function of the position angle, θ , for 1P and 2P stars of NGC 5904. The gray levels are indicative of the density of stars. The red dots and the blue triangles represent the average motions of 1P and 2P stars in angular sectors.

did not detect any significant difference between the amplitudes of the curves of the two populations in the $\Delta\mu_\alpha \cos \delta$ vs. θ plane.

Furthermore, 1P and 2P stars in NGC 5904 are reproduced by sine functions with the same amplitudes. For completeness, we extended the same analysis to NGC 0104 and find no significant difference between the rotation curves of its 1P and 2P stars.

The large number of stars that are available in this cluster allows us to investigate rotation of 1P and 2P stars at different radial distances from the cluster center. We selected two regions with approximately the same number of stars, namely an inner annulus between $\sim 0.8 R_h$ and $\sim 2.4 R_h$ (2.3 to 6.6 arcmin), and an outer annulus that goes from $\sim 2.4 R_h$ to $\sim 5.0 R_h$ (6.6 to 14.0 arcmin), with R_h being the half-light radius listed in Table 1. The inner and outer annulus contain respectively 397/877 and 456/750 1P/2P stars. As expected, the star counts are consistent with a more centrally-concentrated 2P (as previously noticed by Milone et al. 2012 and Cordero et al. 2014).

To investigate the rotation of 1P and 2P stars in the inner and outer region we applied the same method described in Section 4.1 for all 1P and 2P stars. The average motions of stars in the inner and outer region are shown in Figure 10, while the values of A and ϕ of the best-fit sine functions of 1P and 2P stars are listed in Table 2. We find that in the inner region the two populations are consistent with the same

rotation. On the other hand, in the outer region we detect both an amplitude difference ($\Delta A = 1.150$ km/s) and a phase difference ($\Delta\phi = 0.500$ rad), between the curves that fit the observations of 1P and 2P stars in the V_{LoS} vs. θ plane. Only 1%/4% of our simulations produce an amplitude/phase difference greater than the observed one. The observed differences are therefore significant to the $\sim 2.3/\sim 2\sigma$ level.

However, due to the lower number of stars with LoS velocity measurements, we obtain poor quality for the interpolation between the sine function and the observations along the LoS for 1P stars in the inner and outer regions of NCG 0104, as shown by the values of r^2 , listed in the bottom right insets of Figure 8.

4.2. Comparison with theory

Figure 8 suggests that the rotation curves of 1P and 2P stars of NGC 5904 exhibit different phases in the μ_δ vs. θ plane and along the line of sight. On the contrary, the two populations seem to share the same rotation pattern when we consider the $\mu_\alpha \cos \delta$ component of the motion. To shed light on this phenomenon, we further investigate the rotation curves of 1P and 2P stars in NGC 5904 by qualitatively comparing the observations with mock simulated stars. Specifically, we generated two stellar populations composed of 50,000 stars each, by extracting their positions and velocities from a King (1966) model with maxwellian velocity distributions. We then added to the motions of each population a specific rotation pattern characterized by the same amplitude A , and

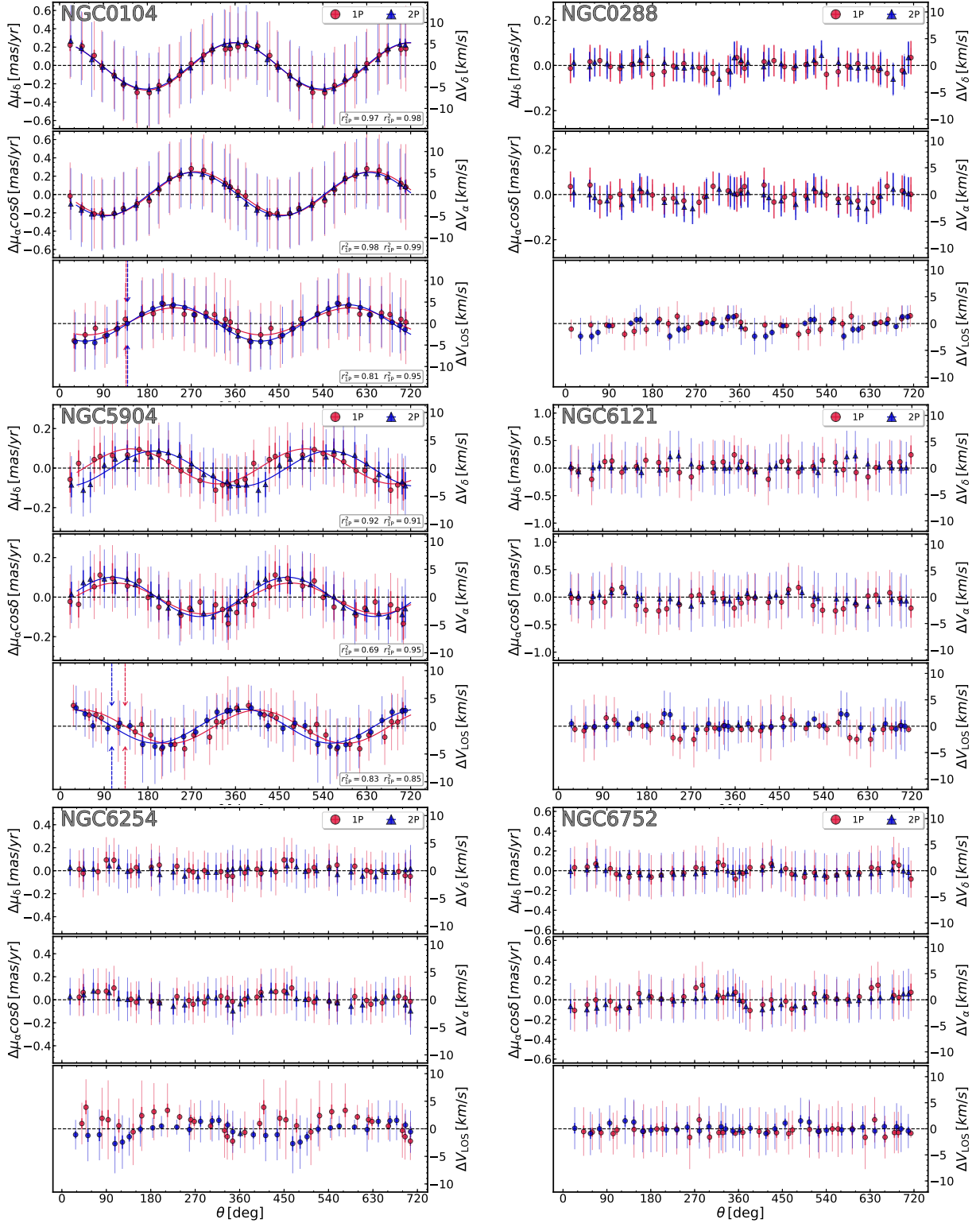


Figure 8. Average proper motions (top and middle panels) and LoS velocities (bottom panels) of 1P (red circles) and 2P stars (blue triangles) as a function of the position angle for 1P and 2P stars of NGC 0104, NGC 0288, NCG 5904, NGC 6121, NGC 6254 and NGC 6752. Thin and thick error bars indicate the uncertainties associated with the average motions and the dispersions, respectively. The red and blue lines superimposed on the plots of NGC 0104 and NGC 5904 are the least-squares best-fit functions of 1P and 2P stars, respectively. The vertical red/blue arrows plotted in the bottom panels highlight the PA of the rotation axis of 1P and 2P stars, determined as the zero of the rotation curve.

ID	field		motion component	ϕ (PA)	A
				rad	mas/yr (km/s)
NGC 0104	1P	all	$\mu_\alpha \cos \delta$	2.96±0.06	0.237±0.007
			μ_δ	1.54±0.07	0.257±0.008
			V_{LoS}	5.53±0.30	3.35±0.35
	2P		$\mu_\alpha \cos \delta$	3.13±0.04	0.236±0.005
			μ_δ	1.61±0.05	0.253±0.006
			V_{LoS}	5.50±0.16	4.23±0.18
NGC 5904	1P	all	$\mu_\alpha \cos \delta$	2.691±0.24	0.078±0.010
			μ_δ	2.254±0.11	0.089±0.007
			V_{LoS}	2.44±0.33	2.69±0.40
	2P		$\mu_\alpha \cos \delta$	2.91±0.11	0.099±0.007
			μ_δ	1.38±0.13	0.089±0.006
			V_{LoS}	1.90±0.19	3.20±0.27
NGC 0104	1P	inner	$\mu_\alpha \cos \delta$	3.10±0.08	0.288±0.013
			μ_δ	1.50±0.14	0.265±0.021
			V_{LoS}	4.40±0.39	4.29±0.57
	2P		$\mu_\alpha \cos \delta$	3.18±0.05	0.289±0.009
			μ_δ	1.60±0.07	0.282±0.008
			V_{LoS}	5.50±0.15	4.70±0.24
NGC 0104	1P	outer	$\mu_\alpha \cos \delta$	2.86±0.08	0.221±0.009
			μ_δ	1.58±0.07	0.285±0.009
			V_{LoS}	5.84±0.45	2.71±0.58
	2P		$\mu_\alpha \cos \delta$	2.92±0.09	0.205±0.008
			μ_δ	1.69±0.08	0.240±0.007
			V_{LoS}	5.34±0.16	3.86±0.20

Table 2. Amplitudes and phases (Position Angle in the case of the line-of-sight component) of the best-fit functions (Equation 1) describing the observations of 1P and 2P stars in the $\mu_\alpha \cos \delta$ vs. θ , μ_δ vs. θ planes and V_{LoS} vs. θ . The upper twelve lines in the Table refer to the entire sample of analyzed 1P and 2P stars of NGC 0104 and NGC 5904, while in the lower twelve lines we consider 1P and 2P stars in the inner and outer fields of NGC 0104.

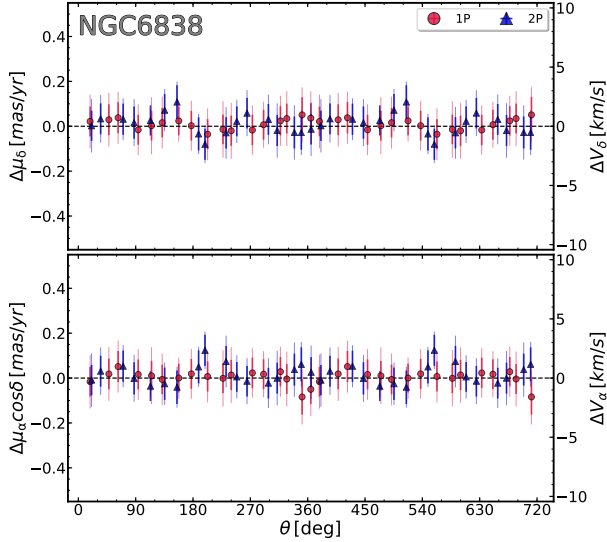


Figure 9. Same as Figure 8 for NGC 6838. LoS velocities are not available for NGC 6838.

different inclination of the rotation axis with respect to the line-of-sight, i , and position angle θ_0 , (as in Sollima et al. 2019, their Equation A1).

We compared the rotation curves of pairs of mock stellar populations with different rotation patterns along the three space directions X, Y and Z. We find that stellar populations with the same amplitudes but different inclinations and phases qualitatively reproduce the observations of NGC 5904. As an example, we show in Figure 11 that two stellar populations with amplitude ($A = 0.4$) inclinations ($i = 80^\circ$ and 120°) and phases ($\phi_0 = 15^\circ$ and 0°) qualitatively reproduce the observed pattern. Indeed the simulated rotation curves along the direction X and Y exhibit different phases, while sharing nearly the same phase along the Z direction.

4.3. Line of sight velocity map

For completeness we compare in Figure 12 the LoS velocity map with the spatial distribution of 1P and 2P stars in NGC 5904. The four panels show the smoothed LoS velocity map, color coded as indicated by the colorbar. The black dashed lines represent the PA of the rotation axis, derived from the rotation curves as explained in Section 4, while the black solid lines are the same isodensity contour lines derived in Section 3. Clearly, the rotation axis is consistent with the minor axis of the best-fit ellipses, as expected for oblate rotators. This agreement is even more important since these quantities, i.e. the PA of the rotation axis and the major/minor axis of the best-fit ellipses, are determined with independent techniques.

5. VELOCITY PROFILES

To study the internal motion of stars as a function of the radial distance from the cluster center we divided the cluster field into different circular annuli, that are determined with the naive estimator method (Silverman 1986).

For each annulus we computed the systematics-corrected median values of the radial ($\Delta\mu_{\text{RAD}}$) and tangential ($\Delta\mu_{\text{TAN}}$) components of proper motions for 1P and 2P stars relative to the corresponding median proper motion components of all stars.

These proper motions have been converted into velocities, ΔV_{RAD} and ΔV_{TAN} , by assuming for each cluster the distances listed in Table 1, from Baumgardt & Hilker (2018).

Figure 13 shows the velocity profiles of the analyzed clusters as a function of the radial distance from the cluster center. To better compare the various clusters we normalized the radial distance from the cluster center to the value of its half-light radius provided by Baumgardt & Hilker (2018) and converted the radial distances from angular to physical units by means of the distances provided in Table 1.

The two populations of most GCs share similar velocity profiles and any difference between the velocities of 1P and 2P stars is smaller than ~ 1 km/s. These conclusions are corroborated by the Anderson-Darling test, which provides the probabilities for 1P and 2P stars to be drawn from the same parent distribution that are quoted in the insets of Figure 13. As a further determination of the statistical significance of the differences between the velocity profiles of 2P and 1P stars we used the following procedure. We computed the χ^2_{obs} between the observed profiles of the 1P and 2P. We then simulated 1,000 profiles for 1P and 2P, where we assumed that the two populations have the same distribution, and we scattered each star according to its observed uncertainty. For each simulation we computed the χ^2_{sim} between 1P and 2P profiles, and we counted the number of realizations for which $\chi^2_{\text{sim}} \gtrsim \chi^2_{\text{obs}}$, (N^*). The ratio between (N^*) and the total number of realizations, (N_{sim}) is indicative of the significance, and it is quoted in the bottom-right corner of each panel in Figure 13.

NGC 5904 seems a remarkable exception. Indeed, in the radial interval between ~ 2 to ~ 5 half-light radii from the center, 1P stars exhibit higher radial motions than 2P stars.

However, such difference would be attributed to systematics as suggested by the high ratio $N^*/N_{\text{sim}} = 0.21$. Improved proper motions, as those from next GAIA data releases, are mandatory to understand whether the observed difference is real or not.

5.1. Velocity dispersions of 1P and 2P stars

To derive the velocity dispersion of 1P and 2P stars in each annulus we followed the procedure described in Mackey et al. (2013) and Marino et al. (2014). Briefly we considered

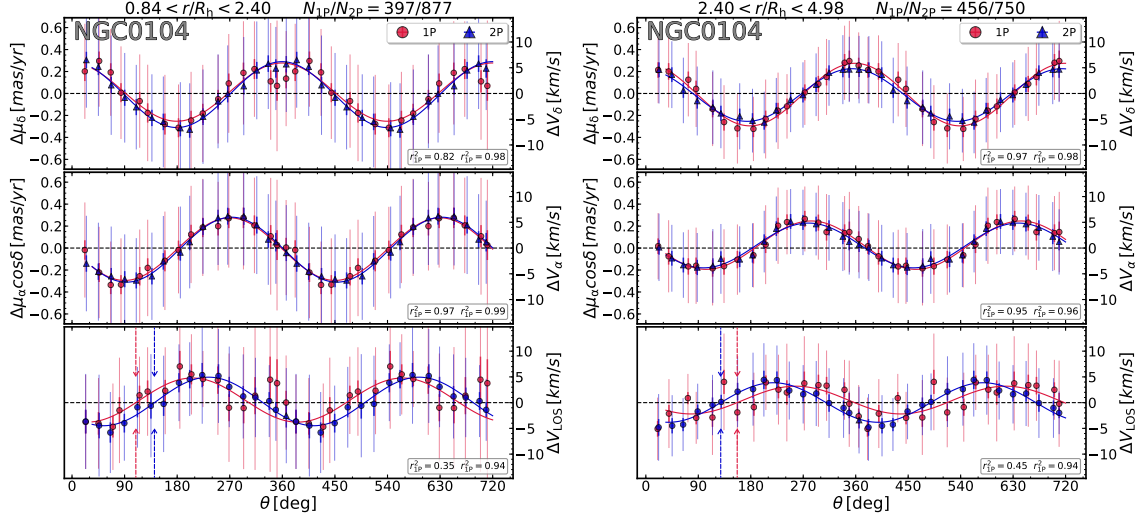


Figure 10. Same as Figure 8 for stars in the inner (left panel) and outer (right panel) regions of NGC 0104. The curves are the best-fit sine functions. Red and blue colors refer to 1P and 2P stars, respectively. See text for details.

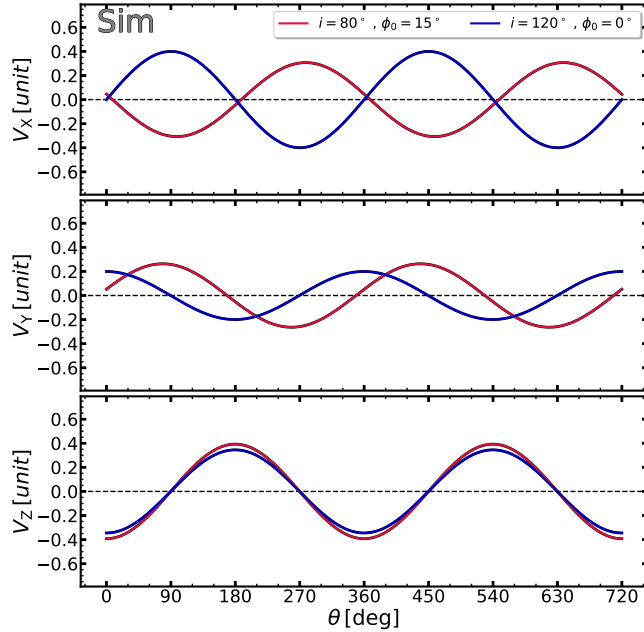


Figure 11. Projected motions along three space directions, X, Y and Z, of two simulated stellar populations with different rotation patterns. See text for details.

the negative log-likelihood function:

$$\lambda = \prod_{i=1}^N p(v_i, \epsilon_i)$$

with the probability of finding a star with velocity v_i and uncertainty ϵ_i given by:

$$p(v_i, \epsilon) = \frac{1}{2\pi \sqrt{(\sigma^2 + \epsilon_i^2)}} \exp\left(-\frac{(v_i - v)^2}{2(\sigma^2 + \epsilon_i^2)}\right)$$

and we found the intrinsic dispersion by maximizing the likelihood. Again, the uncertainties associated with each point are determined by bootstrapping with replacements performed 1,000 times. Figure 14 shows the velocity dispersion profile for the studied clusters, where the radial coordinated has been normalized to the half-light radius from Baumgardt & Hilker (2018).

We computed the quantity $\sigma_{\text{TAN}}/\sigma_{\text{RAD}} - 1$, which is indicative of the anisotropy of the internal motion, and show its radial profile in Figure 15. The horizontal lines in the plots correspond to isotropic stellar systems. As a global and independent measure of the degree of anisotropy, we determined, for each population, the ratio between the radial kinetic energy and the total kinetic energy, $k = \epsilon_{\text{RAD}}/(\epsilon_{\text{TAN}} + \epsilon_{\text{RAD}})$. The results are listed in bottom-right corners of Figure 15. As expected, non rotating clusters are characterized by a value of k close to $k = 0.5$, expected for isotropic stellar systems. On the other hand, NGC 0104 and NGC 5904 show a higher degree of tangential anisotropy, as a consequence of the non-zero tangential velocity. We confirm that NGC 0104 exhibits strong differences in the degree of anisotropy of the two populations, with the 2P being more radially anisotropic than the 1P. The external region of NGC 5904 shows hints of a more radially anisotropic 2P, but the large uncertainties prevent us from any further discussion.

The remaining clusters are consistent with being isotropic

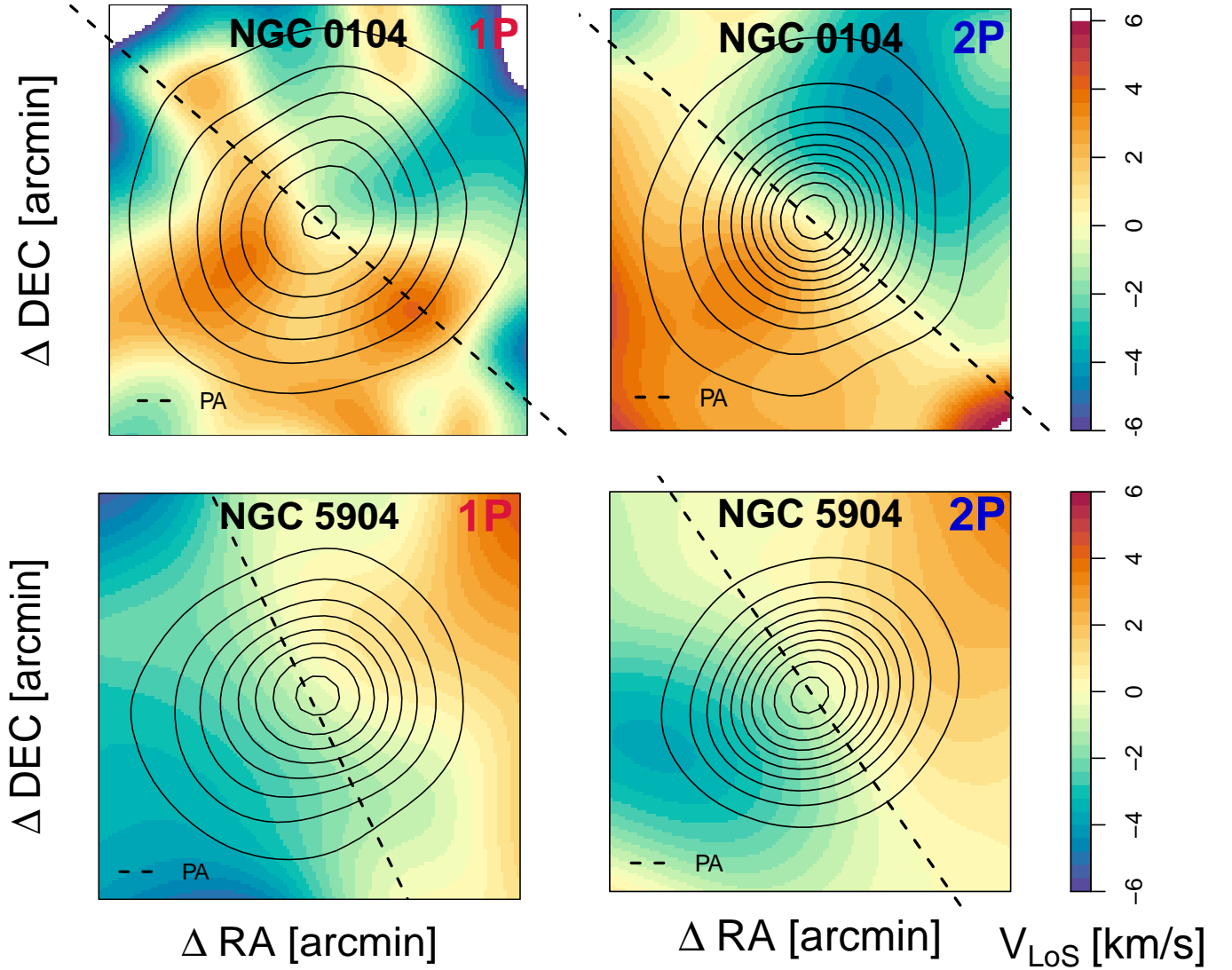


Figure 12. Line-of-sight velocity map of different stellar populations in NGC 0104, top panels, and NGC 5904, bottom panels. Superimposed are the isodensity contour lines, derived in Section 3. The thick black dashed line represents the position angle of the rotation axis, as determined in Section 4. The colorbars on the right indicate the LoS velocity in km/s.

stellar systems. Concerning the LoS velocity dispersion profile we find some differences in NGC 0104, in the outermost part of NGC 5904 and also in NGC 6254.

6. SUMMARY AND DISCUSSION

We exploited Gaia DR2 proper motions and parallaxes of stars in the field of views of seven GCs, namely NGC 0104, NGC 0288, NGC 5904, NGC 6121, NGC 6254, NGC 6752 and NGC 6838 to separate cluster members from field stars. We analyzed the V vs. $C_{U,B,I}$ diagrams corrected for differential reddening of clusters members to identify 1P and 2P stars along the RGB and study their spatial distributions and

internal kinematics by using Gaia DR2 stellar positions and proper motions and ESO/VLT and Keck LoS velocities. To our knowledge, this is the first homogeneous study of the three velocity component internal kinematics of distinct stellar populations in a large sample of GCs over a wide field of view.

We find that 1P and 2P stars of NGC 0104, NGC 5904 and NGC 6254 exhibit different spatial distributions. Specifically, in NGC 5904 and NGC 6254 2P stars exhibit higher ellipticities than the 1P, while NGC 0104 seems consistent with a more-elliptical 1P. The two populations of the other clusters share the same spatial distribution. The entire sample of an-

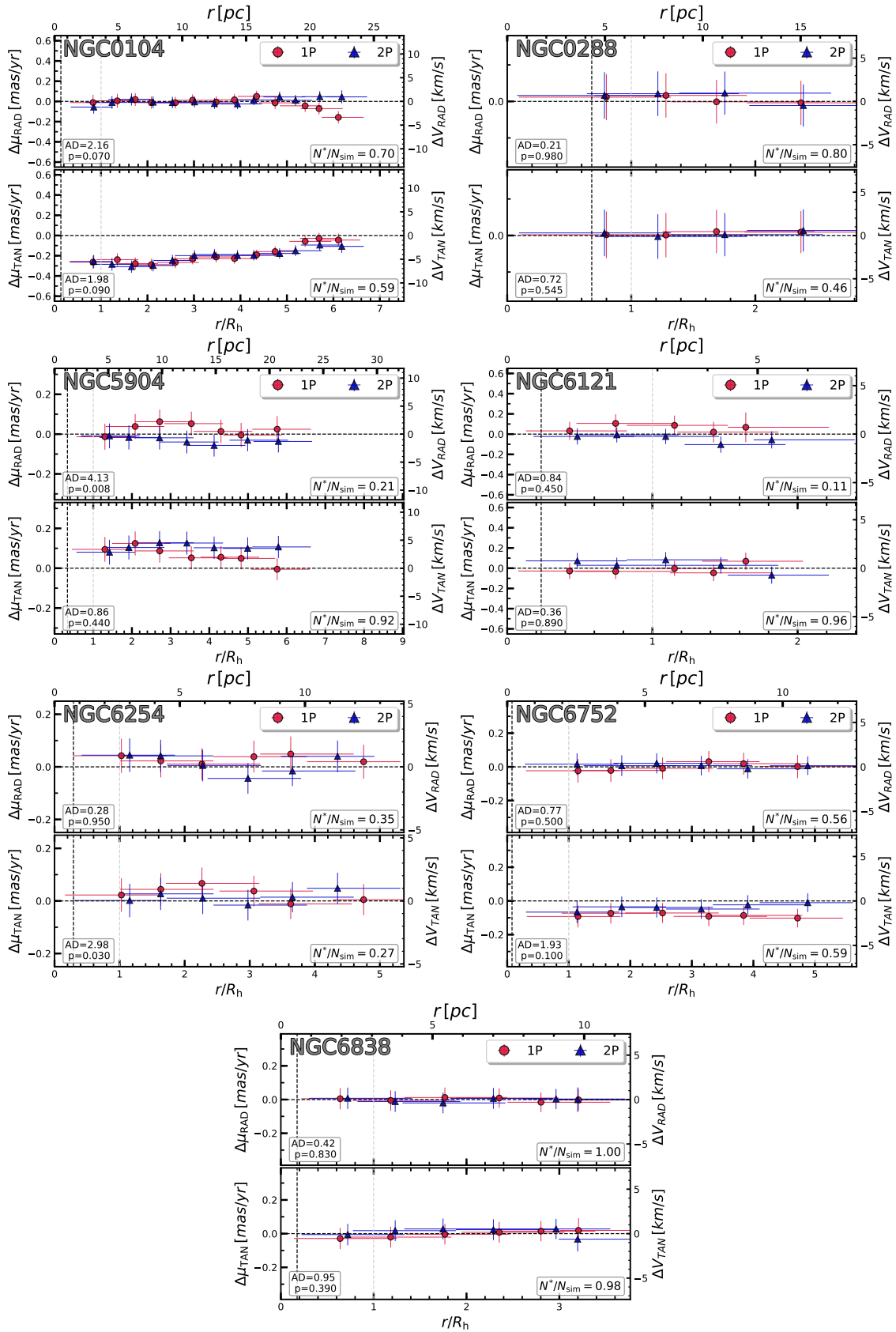


Figure 13. Average tangential and radial motions for NGC 0104, NGC 0288, NGC 5904, NGC 6121, NGC 6254, NGC 6752 and NGC 6838 as a function of the radial distance from the cluster center. The radial coordinate is normalized to the half-light radius from Baumgardt & Hilker (2018). Horizontal lines mark the radial extension of the radial bins. The black and gray dashed lines indicate the core and the half-light radius, respectively. We quote for each cluster the probability, p , of the velocity distribution of 1P and 2P stars to be drawn from the same parent distribution according to the Anderson-Darling test (AD, Scholz et al. 1987). In the bottom-right corner of each panel is shown the significance of the differences between the median profile of 1P and 2P, computed as explained in the text.

ID	field	motion component	A-D	p-val	ΔA^{obs} mas/yr (km/s)	$\Delta\phi^{\text{obs}}$ rad	$P(\Delta A^{\text{sim}} \geq \Delta A^{\text{obs}})$	$P(\Delta\phi^{\text{sim}} \geq \Delta\phi^{\text{obs}})$
NGC 0104	all	$\mu_{\alpha} \cos\delta$	1.53	0.17	0.001 ± 0.020	0.160 ± 0.090	0.960	0.083
		μ_{δ}	1.59	0.16	0.004 ± 0.022	0.070 ± 0.080	0.104	0.460
		V_{LoS}	1.59	0.16	0.88 ± 0.40	0.030 ± 0.280	0.390	0.281
NGC 5904	all	$\mu_{\alpha} \cos\delta$	2.62	0.05	0.020 ± 0.020	0.224 ± 0.195	0.260	0.170
		μ_{δ}	3.00	0.03	0.000 ± 0.018	0.870 ± 0.224	0.951	0.008
		V_{LoS}	1.59	0.16	0.51 ± 0.48	0.541 ± 0.200	0.453	0.021
NGC 0104	inner	$\mu_{\alpha} \cos\delta$	1.44	0.20	0.001 ± 0.038	0.080 ± 0.134	0.980	0.503
		μ_{δ}	0.59	0.66	0.017 ± 0.039	0.100 ± 0.125	0.422	0.434
		V_{LoS}	1.59	0.16	0.41 ± 0.50	0.533 ± 0.410	0.550	0.062
NGC 0104	outer	$\mu_{\alpha} \cos\delta$	2.54	0.05	0.016 ± 0.026	0.060 ± 0.121	0.532	0.593
		μ_{δ}	1.98	0.10	0.044 ± 0.028	0.110 ± 0.103	0.100	0.402
		V_{LoS}	1.59	0.16	1.15 ± 0.62	0.500 ± 0.500	0.010	0.041

Table 3. Comparison of the rotation curves in the $\mu_{\alpha} \cos\delta$ vs. θ , μ_{δ} vs. θ and V_{LoS} vs. θ planes of 1P and 2P stars in the entire field of view of NGC 0104 and NGC 5904 and in the inner and outer region of NGC 0104. We provide the A-D values from the Anderson-Darling test and the corresponding probability that 1P and 2P stars comes from the same parent distribution (p-val). We list the amplitude (ΔA^{obs}) and phase differences ($\Delta\phi^{\text{obs}}$) of the curves that provide the best-fit with 2P and 1P stars and the probability that the observed difference in phase and amplitude are due to observational errors as inferred from Monte-Carlo simulations.

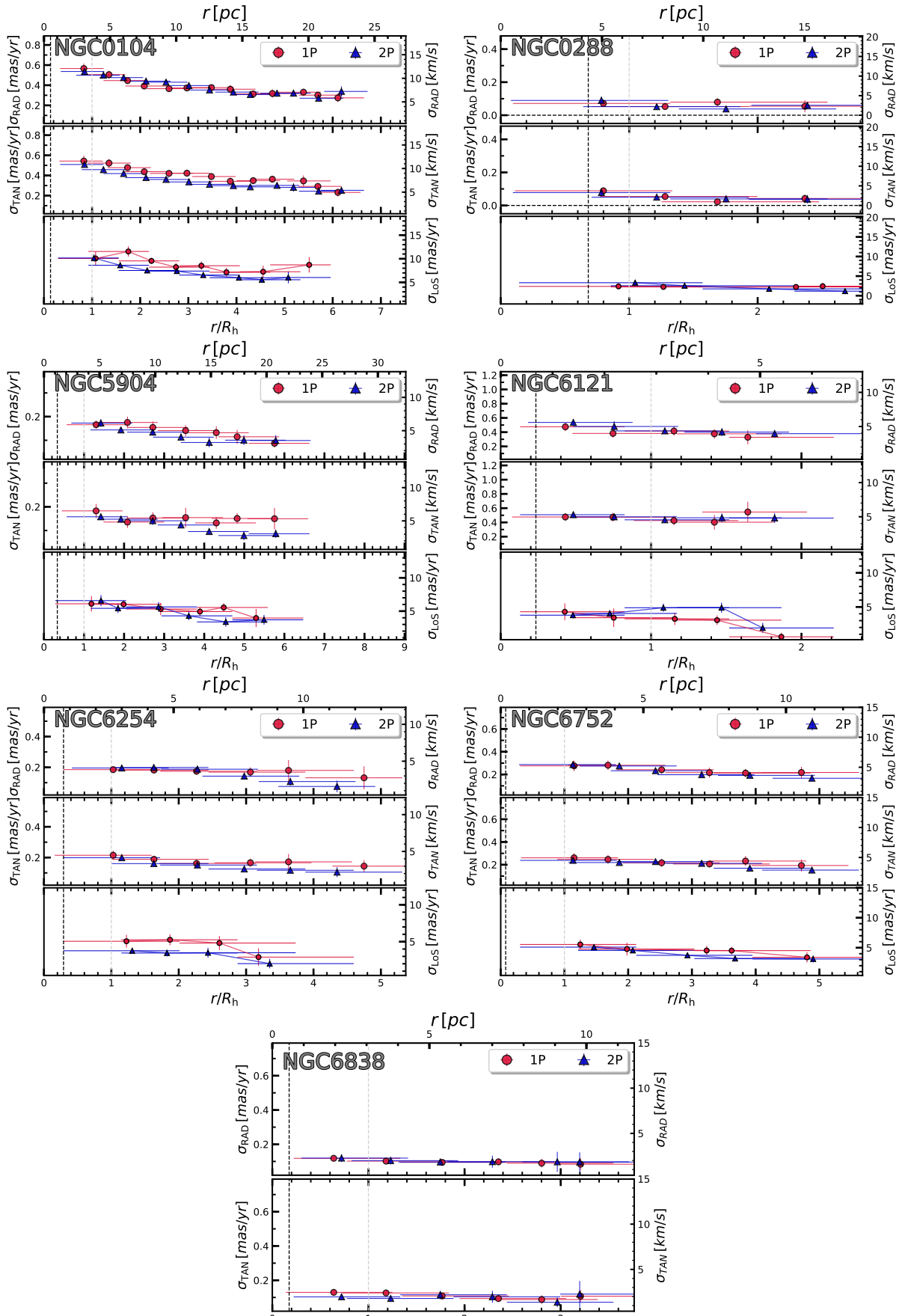


Figure 14. Velocity dispersion profiles for the radial, tangential and LoS velocity, for the analyzed GCs, except NGC 6838 for which LoS velocities are not available. As in Figure 13, the radial coordinates have been normalized to the half-light radius. Black and gray dashed lines mark the core and the half-light radius, respectively.

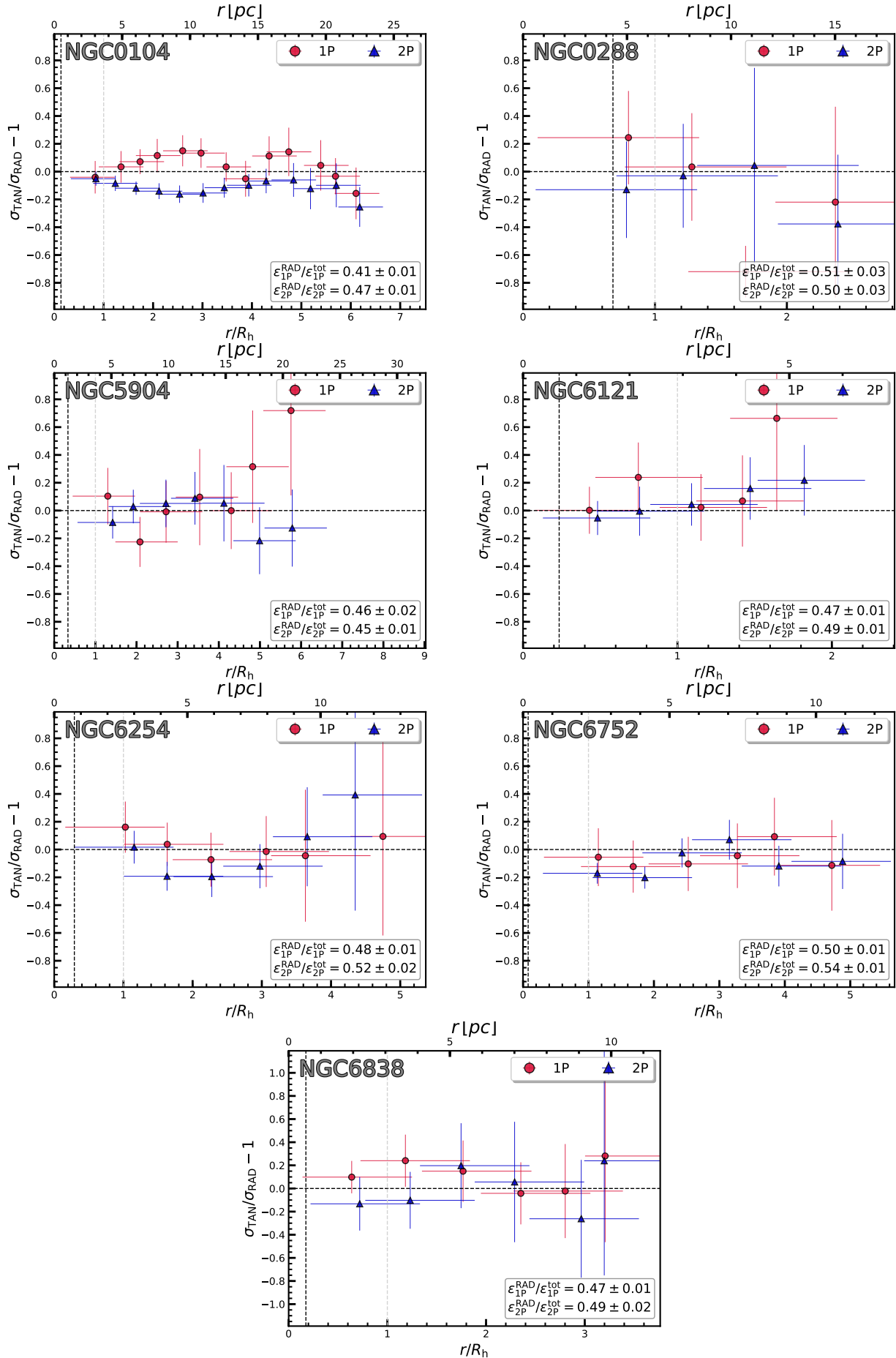


Figure 15. Anisotropy profiles for the analyzed clusters. The radial coordinate is normalized to the half-light radius from Baumgardt & Hilker (2018). Black and gray dashed lines represent the core- and the half-light radius.

alyzed 1P and 2P stars of NGC 0104 share similar rotation patterns and that 2P stars show stronger anisotropies than the 1P stars thus corroborating previous findings from our group (Milone et al. 2018). When we divide stars of NGC 0104 into two annuli with different radial distances, we find that the sine functions that best reproduce the rotation curves 1P and 2P exhibit different phases and amplitudes in the LoS component. However, such difference is significant at $2\text{-}\sigma$ level only.

We confirm that NGC 0104 and NGC 5904 exhibit strong rotation both in the plane of the sky (Anderson & King 2003; Bianchini et al. 2018; Milone et al. 2018; Sollima et al. 2019) and along the line-of-sight (Kamann et al. 2018; Lanzoni et al. 2018).

Lee (2017) studied multiple populations in NGC 5904 by using ground-based on Ca-CN photometry. He separated 1P and 2P along the RGB by using the V vs. cn_{JWL} diagram, which is a powerful tool to identify stellar populations with different nitrogen abundances along the RGB. Lee used the radial velocities of 100 stars by Carretta et al. (2009) to investigate the projected rotations of the two populations identified photometrically. He found that 2P has a substantial net projected rotation whereas there is no evidence for any net projected rotation of 1P stars.

Our results, based on Gaia DR2 proper motions of 263 1P and 535 2P stars and Eso/VLT LoS velocities of 106 and 238 1P/2P stars, show that both populations exhibit significant rotation along the plane of the sky and the line of sight. The sine functions that describe rotation of 2P and 1P stars exhibit different phases in the $\Delta\mu_\delta$ vs. θ and in the V_{LoS} vs. θ planes and such differences are significant at the $\sim 2.6\text{-}\sigma$ and $\sim 2.3\text{-}\sigma$ level, respectively. The two populations exhibit the same phase when we consider the rotation in the $\Delta\mu_\alpha \cos\delta$ vs. θ plane. Such rotation pattern is qualitatively consistent with different position angles and inclinations of the rotation axis.

Our analysis confirms no evidence of rotation in NGC 0288, NGC 6121, NGC 6254 and NGC 6838 (e.g. Bianchini et al. 2018; Sollima et al. 2019). On the other hand, our results are in apparent disagreement with the conclusion by Bianchini and collaborators who detected a significant rotation of NGC 6752 stars in the plane of the sky. We attribute the discrepancy to the small sample of 1P and 2P NGC 6752 stars studied in our paper. We verified that, when we extend our analysis to all the stars of NGC 6752 as done by Bianchini et al. (2018) and Sollima et al. (2019) we confirm previous evidence of rotation.

There is no significant difference between the tangential and radial motions of 1P and 2P stars in the analyzed clusters. 1P stars of NGC 5904 seem to exhibit, on average, larger motions in the radial direction than 2P stars in the region between ~ 2 and 5 half-light radii from the cluster center but

such difference is not statistically significant when we account for systematic errors in Gaia DR2 proper motions.

We investigate the velocity-dispersion profile of multiple populations in all the GCs and confirm that 2P stars of NGC 0104 show significant anisotropy with respect to the 1P. In the other clusters there is no evidence for strong anisotropy among 1P and 2P stars, with NGC 6121 being a possible exception.

To summarize our results, we find significant kinematical differences in NGC 0104 and NGC 5904, while the remaining clusters are consistent with the presence of multiple stellar populations sharing the same internal dynamic. It is worth mentioning that these two clusters have the highest values for the half-mass relaxation time in our sample (listed in Table 1), with the exception of NGC 0288. Finally, these results are consistent with the criterion in Hénault-Brunet et al. (2015). According to the authors, multiple stellar populations are not expected to be fully mixed if the relation in Equation 3 is satisfied.

$$M \gtrsim 10^5 M_\odot \cdot \left(\frac{4 \text{ kpc}}{R_G} \right) \quad (3)$$

where R_G is the Galactocentric radius, listed in Table 1. Among the clusters in our sample, only NGC 6121 and NGC 6838 do not fulfill Equation 3, and indeed we do not find significant dynamical differences between the 1P and 2P in these two clusters.

All our findings constitute strong constraints for existing and future multiple population scenarios. Self-enrichment scenarios, and in particular the AGB scenario, seem to be able to produce different spatial distributions and kinematics between the first and second generation. This scenario, which is the one that has been studied more in detail in terms of dynamics, predicts a higher central concentration for the 2P with respect to 1P stars. 1P stars have a higher velocity dispersion compared to 2P stars and they show a smaller amount of radial anisotropy. If the 1P cluster is initially rotating, the 2P will form in a centrally concentrated disc and will initially rotate faster than 1P stars. All these signatures are washed out but the two-body relaxation of the clusters. Rotational difference could therefore be absent due to the relaxation process in the velocity space.

Further tests and dynamical models exploring a larger phase-space of the parameters are necessary to understand if the AGB scenario, or any of the other proposed 2P formation mechanisms, are able to reproduce simultaneously all the observed features.

ACKNOWLEDGMENTS

We thank the anonymous referee for his/her helpful suggestions that improved the quality of our work. We would also like to thank Paolo Bianchini, Vincent Hénault-Brunet, Antonio Sollima, Maria Tiongco, Eugene Vasiliev and Enrico Vesperini

for their helpful comments and suggestions. This work has received funding from the European Research Council (ERC) under the European Union's Horizon 2020 research innovation programme (Grant Agreement ERC-StG 2016, No 716082 'GALFOR', PI: Milone, <http://progetti.dfa.unipd.it/GALFOR>), and the European Union's Horizon 2020 research and innovation programme

under the Marie Skłodowska-Curie (Grant Agreement No 797100, beneficiary: Marino). APM and MT acknowledge support from MIUR through the FARE project R164RM93XW SEMPLICE (PI: Milone). AMB acknowledges support by Sonderforschungsbereich (SFB) 881 'The Milky Way System' of the German Research Foundation (DFG).

REFERENCES

- Anderson, J., & King, I. R. 2003, *AJ*, 126, 772
- Baumgardt, H., & Hilker, M. 2018, *MNRAS*, 478, 1520
- Bastian, N., Lamers, H. J. G. L. M., de Mink, S. E., et al. 2013, *MNRAS*, 436, 2398
- Bellazzini, M., Bragaglia, A., Carretta, E., et al. 2012, *A&A*, 538, A18
- Bellini, A., Vesperini, E., Piotto, G., et al. 2015, *ApJL*, 810, L13
- Bellini, A., Libralato, M., Bedin, L. R., et al. 2018, *ApJ*, 853, 86
- Bianchini, P., van der Marel, R. P., del Pino, A. et al. 2018, *MNRAS*, 481, 2125
- Carretta, E., Bragaglia, A., Gratton, R. G., et al. 2009, *A&A*, 505, 117
- Cordero, M. J., Pilachowski, C. A., Johnson, C. I., et al. 2014, *ApJ*, 780, 94
- Cordero, M. J., Hnault-Brunet, V., Pilachowski, et al. 2017, *MNRAS*, 465, 3515
- Cordoni, G., Milone, A. P., Marino, A. F., et al. 2018, *ApJ*, 869, 139
- D'Ercole, A., D'Antona, F., Ventura, P. et al. 2010, *MNRAS*, 407, 854
- de Mink, S. E., Pols, O. R., Langer, N. et al. 2009, *A&A*, 507, L1
- Decressin, T., Meynet, G., Charbonnel, C., Prantzos, N., & Ekström, S. 2007, *A&A*, 464, 1029
- Denissenkov, P. A., & Hartwick, F. D. A. 2014, *MNRAS*, 437, L21
- Glantz, Stanton A.; Slinker, B. K. (1990). *Primer of Applied Regression and Analysis of Variance*. McGraw-Hill. ISBN 978-0-07-023407-9.
- Halir, R. & Flusser, J. (1998). *Numerically Stable Direct Least Squares Fitting Of Ellipses*.
- Harris, W. E. 1996, *AJ*, 112, 1487
- Hénault-Brunet, V., Gieles, M., Agertz, O., & Read, J. I. 2015, *MNRAS*, 450, 1164
- Gaia Collaboration, Brown, A. G. A., Vallenari, A., et al. 2018, *A&A*, 616, A1
- Gaia Collaboration, Helmi, A., van Leeuwen, F., et al. 2018, *A&A*, 616, 12P
- Gieles, M., Charbonnel, C., Krause, M. G. H. et al. 2018, *MNRAS*, 478, 2461
- Kamann, S., Husser, T.-O., Dreizler, S., et al. 2018, *MNRAS*, 473, 5591
- King, I. R. 1966, *AJ*, 71, 64
- Landolt, A. U. 1992, *AJ*, 104, 340
- Lanzoni, B., Ferraro, F. R., Mucciarelli, A., et al. 2018, *ApJ*, 861, 16
- Lee, J.-W. 2017, *ApJ*, 844, 77
- Libralato, M., Bellini, A., van der Marel, R. P., et al. 2018, *ApJ*, 861, 99
- Libralato, M., Bellini, A., Piotto, G., et al. 2019, *ApJ*, 873, 109
- Lindegren, L., Hernández, J., Bombrun, A., et al. 2018, *A&A*, 616, A2
- Mackey, A. D., Da Costa, G. S., Ferguson, A. M. N., & Yong, D. 2013, *ApJ*, 762, 65
- Marino, A. F., Milone, A. P., Yong, D., et al. 2014, *MNRAS*, 442, 3044
- Marino, A. F., Milone, A. P., Casagrande, L., et al. 2016, *MNRAS*, 459, 610
- Marino, A. F., Milone, A. P., Yong, D., et al. 2017, *ApJ*, 843, 66
- Marino, A. F., Milone, A. P., Renzini, A., et al. 2019, *MNRAS*, 487, 3815
- Mastrobuono-Battisti, A., & Perets, H. B. 2013, *ApJ*, 779, 85
- Mastrobuono-Battisti, A., & Perets, H. B. 2016, *ApJ*, 823, 61
- Milone, A. P., Piotto, G., Bedin, L. R., et al. 2012, *A&A*, 540, A16
- Milone, A. P., Piotto, G., Bedin, L. R., et al. 2012, *ApJ*, 744, 58
- Milone, A. P., Marino, A. F., Piotto, G., et al. 2015, *ApJ*, 808, 51
- Milone, A. P., Piotto, G., Renzini, A., et al. 2017, *MNRAS*, 464, 3636
- Milone, A. P., Marino, A. F., Mastrobuono-Battisti, A., & Lagioia, E. P. 2018, *MNRAS*, 479, 5005
- Monelli, M., Milone, A. P., Stetson, P. B., et al. 2013, *MNRAS*, 431, 2126
- Norris, J. E., Freeman, K. C., Mayor, M., & Seitzer, P. 1997, *ApJL*, 487, L187
- Pancino, E., Galfo, A., Ferraro, F. R., & Bellazzini, M. 2007, *ApJL*, 661, L155
- Halir, R. & Flusser, J. 1998
- Renzini, A., D'Antona, F., Cassisi, S., et al. 2015, *MNRAS*, 454, 4197
- Richer, H. B., Heyl, J., Anderson, J., et al. 2013, *ApJL*, 771, L15
- Scholz, Fritz W. & Stephens, Michael A., 1987, *Journal of the American Statistical Association*, 82, 399
- Silverman B. W., 1986, *Monographs on Statistics and Applied Probability*. Chapman and Hall, London
- Sollima, A., Baumgardt, H., Hilker, M., 2019, *MNRAS*, 485, 1460
- Stetson, P. B. 2005, *PASP*, 117, 563

- Stetson, P. B., Pancino, E., Zocchi, A. et al. 2019, MNRAS, 485, 3042
- Tiongco, M. A., Vesperini, E. & Varri, A. L. 2019 MNRAS, 487, 5535
- van de Ven, G., van den Bosch, R. C. E., Verolme, E. K., & de Zeeuw, P. T. 2006, A&A, 445, 513
- Vasiliev, E. 2019, MNRAS, 484, 2832
- Vasiliev, E. 2019, MNRAS, 489, 623
- Ventura, P., D'Antona, F., Mazzitelli, I., & Gratton, R. 2001, ApJL, 550, L65
- Vesperini, E., McMillan, S. L. W., D'Antona, F., & D'Ercole, A. 2013, MNRAS, 429, 1913
- Wand, M. 2015, KernSmooth: Functions for Kernel Smoothing Supporting Wand & Jones (1995)